Chapter 2
Primary Minerals

Abstract This chapter introduces the primary minerals that are relatively common in soils. It first presents the accepted views on the elemental compositions of the Earth's crust, rocks, and minerals. Soils at the top of the Earth's crust are also within the rock cycle. Silicate and silica minerals, which constitute more than 90% of the minerals in the Earth' crust, are outlined. Samples of relatively un-weathered and weathered primary minerals were obtained from new volcanic ash and soils derived from granitic rocks, respectively. Quartz is highly resistant to weathering, whereas biotite in soil is altered in moist climates. The composition of primary minerals in soils is affected by the types of parent rocks, weathering, sorting, and other soil-forming factors, resulting in mineral compositions that deviate from the average mineral composition of the Earth's crust.

2.1 Introduction

Ranging from clay to rock fragment, soil particles have a wide size distribution. Minerals in soils are divided conceptually into primary and secondary minerals. According to the Glossary of Soil Science Terms (Glossary of soil science terms committee 2008), a primary mineral is a mineral that has not been altered chemically since its crystallization from molten lava and deposition. A mineral is defined as an inorganically formed, naturally occurring homogeneous solid with a definite chemical composition and an ordered atomic arrangement. These definitions are followed in this monograph.

Soils form by widely different processes, and their states range from un-weathered to highly weathered. They thus show various compositions of primary and secondary materials. The particle-size fraction of most primary minerals is the larger than 2 μm fraction, which includes silt, sand, and gravel. Primary minerals can be separated from soil by the particle-size fractionation method described in the Sect. 1.4.

The major primary minerals in soil are silicate and silica minerals. Other minerals include titanomagnetite, other iron minerals, and apatite. The sand fraction of soils

M. Nanzyo, H. Kanno, *Inorganic Constituents in Soil*,
https://doi.org/10.1007/978-981-13-1214-4_2

includes non-crystalline inorganic constituents, such as volcanic glasses. Volcanic glasses and apatite are introduced in Chap. 4 and Sect. 6.3, respectively.

Particles larger than silt includes fine rock fragments, complex particles of different minerals, and partially weathered minerals. After introducing the major primary minerals in soils, this chapter exemplifies the mineral composition of fine rock fragments on a polished section, and partially weathered minerals.

2.2 Average Mineral Composition of the Earth's Crust

Earth's surface is naturally mobile. The mobile layer is made up of plates comprising the Earth's crust and uppermost mantle. On average, the Earth's crust is 40 km thick on continents and 6 km thick in the oceans. The upper mantle consists mainly of peridotite, whereas the crust consists of igneous rocks, sedimentary rocks, and metamorphic rocks (Fig. 2.1). These three rock families of the Earth's crust can interchange through diastrophism (the rock cycle, Fig. 2.2) (Skinner and Mruck 2011). The phases of the rock cycle can undertake various shortcuts. The rock cycle is active in the subduction zone of a plate and in the collision zones of continents, but it is relatively inactive in stable continental crust. However, on the surface of the continental crust, soil formation processes are continuously active.

According to the estimated average element composition of the Earth's crust, oxygen is the most abundant element, followed by Si and Al (see Fig. 2.1). The crust consists of 65% igneous rocks, 27% metamorphic rocks, and 8% sedimentary rocks (Fig. 2.1). Approximately two-thirds of the igneous rocks are basic rocks; neutral and acidic rocks constitute approximately one-sixth each. The very surface of the Earth's crust is dominated by sedimentary rocks, which are strongly affected by weathering, erosion, transportation, and deposition (Fig. 2.2).

The rocks of the Earth's crust are dominated by plagioclase, followed by quartz, alkali feldspar, and other silicates. Collectively, these minerals constitute approximately 92% of the rock material (Fig. 2.1). Other minerals are non-silicate minerals such as carbonates, sulfates, phosphates, sulfides, fluorides, and chlorides. The alteration of rocks and minerals depends on the soil formation factors, which vary across the surface of the Earth.

2.3 Silicate and Silica Minerals

2.3.1 Grouping of Silicate and Silica Minerals

Silicate and silica minerals are grouped into six types based on the bonding structure of their silicate tetrahedrons. Examples and the ideal chemical formulas of the six types of silicates are summarized in Table 2.1. The model structures of five silicate types are shown in Fig. 2.3. Nesosilicates are characterized by single SiO_4 tetrahedra

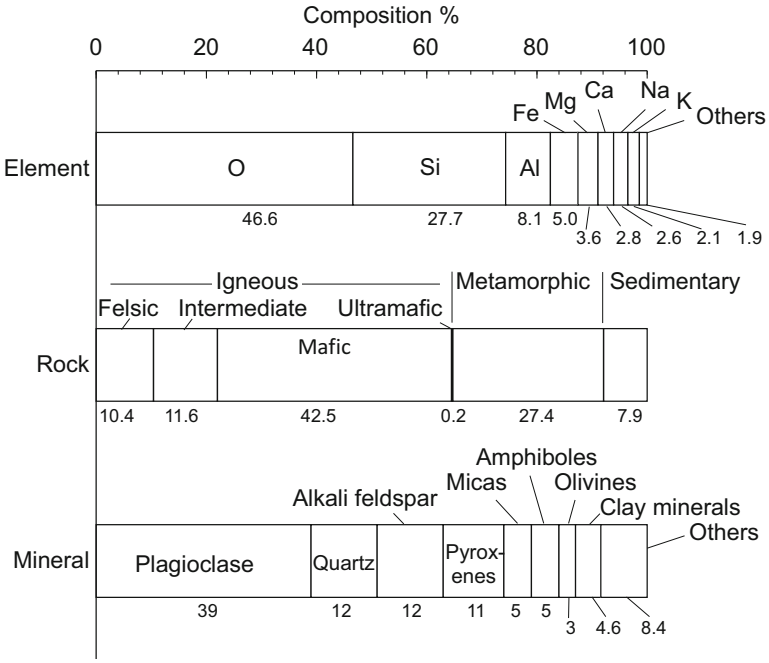

Fig. 2.1 Average element and rock and mineral (Wyllie 1971) compositions of the Earth's crust

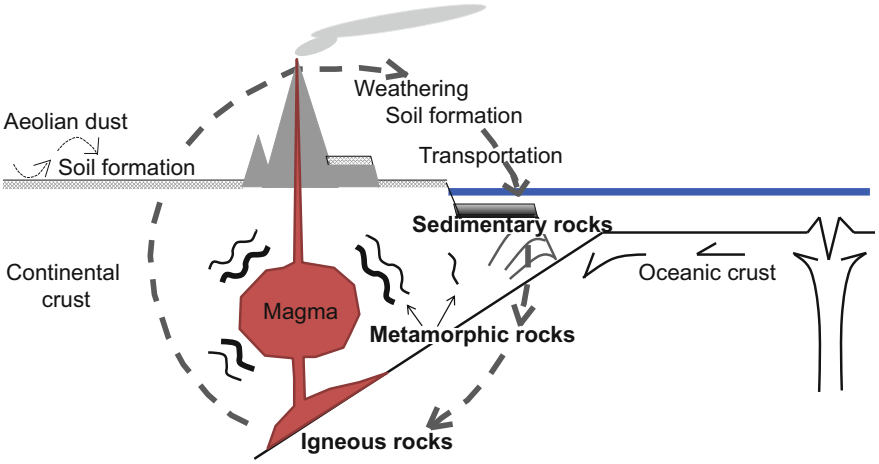

Fig. 2.2 Schematic of the rock cycle. Various shortcuts are possible in this cycle

with no Si–O–Si bonding. Other silicates are constructed from units of two or more connected SiO_4 tetrahedra. Sorosilicates are dimers of SiO_4 tetrahedra. Cyclosilicates have a ring structure composed of 3–6 SiO_4 tetrahedra. Inosilicates

Table 2.1 Grouping of silicate and silica minerals

	Subclass name	Characteristics		Example	Ideal formula
1	Nesosilicates	Lone tetrahedron	$[SiO_4]^{4-}$	Olivine	$(Mg, Fe^{2+})_2SiO_4$
2	Sorosilicates	Double tetrahedra	$[Si_2O_7]^{6-}$	Vesuvianite	$Ca_{19}(Al, Fe)_{10}(Mg, Fe)_3(Si_2O_7)_4(SiO_4)_{10}(O, OH, F)_{10}$
3	Cyclosilicates	Ring silicates	$[Si_nO_{3n}]^{2n-}$	Tourmaline	$NaMg_3Al_6(Si_6O_{18})(BO_3)_3(OH)_3(OH, F)$ (dravite)
4	Inosilicates	Single chain silicates	$[Si_nO_{3n}]^{2n-}$	Pyroxene	$(Ca, Mg, Fe^{2+}, Al)_2(Si, Al)_2O_6$ (augite)
		Double chain silicates	$[Si_{4n}O_{11n}]^{6n-}$	Amphibole	$Ca_2(Mg, Fe^{2+})_4$ Al $[Si_7Al]O_{22}(OH)_2$ (magnesiohornblende)
5	Phyllosilicates	Sheet silicates	$[Si_{2n}O_{5n}]^{2n-}$	Muscovite	$K_2Al_4(Si_6Al_2)O_{20}(OH)_4$
				Biotite	$K_2(Mg, Fe)_6(Si_6Al_2)O_{20}(OH)_4$
				Clay minerals	See Chap. 3
6	Tectosilicates	3D framework	$[Al_xSi_yO_{2(x+y)}]^{x-}$	Quartz	SiO_2
				Feldspar	$NaAlSi_3O_8$ (albite)

consist of linear chains of SiO_4 tetrahedra. The chains may be single or double. In phyllosilicates, the SiO_4 tetrahedra are assembled into 6-membered rings, which connect and spread two-dimensionally into a sheet-like structure. Tectosilicates are three-dimensional assemblages of SiO_4 tetrahedra. In soils, nesosilicates, inosilicates, phyllosilicates, and tectosilicates are common to abundant and present as primary and clay minerals. Allophane and imogolite are also grouped in the nesosilicates, although these two are non-crystalline.

2.3.2 Examples of Silicate and Silica Minerals in Soil

This section presents examples of the silicate and silica minerals frequently found in soils. Several examples of un-weathered mineral particles were taken from new volcanic ash deposits. Partially weathered minerals are so common in soils that a few examples of them are also included in this section.

2.3.2.1 Silicate Minerals

Silicate minerals are various salts of silicate anions (Fig. 2.3). The cations are Al, Mg, Fe, Ti, Na, K, Ca, and other elements. In the following discussion, the silicate minerals are introduced in order of increasing complexity of their silicate framework.

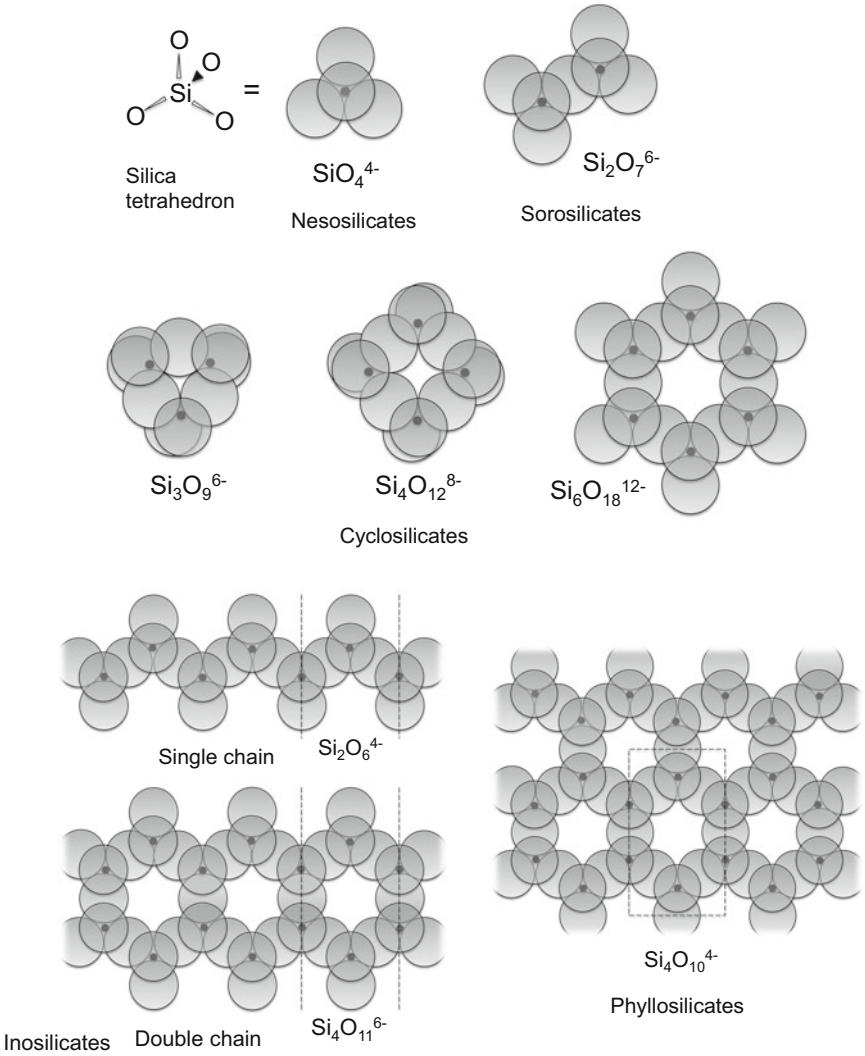

Fig. 2.3 Model structures of silicate and silica minerals. For tectosilicates, refer to Deer et al. (2013)

The minerals are characterized by their EDX spectra and the X-ray diffraction (XRD) patterns of their powder samples. These data are presented along with an optical micrograph and an SEM image of each mineral. The SEM images show the detailed morphological properties of the material. Reference EDX spectra-mimic graphs showing the reference elemental compositions (atomic number ratios) of each mineral are also provided. The horizontal axes of the EDX spectra-mimic graphs are matched with those of the EDX spectra so that readers can easily compare the exemplified mineral with the reference data.

Olivine

Olivine is a light-yellow to yellow-brown or olive-green nesosilicate (Fig. 2.4a). It is sometimes found in basic rocks or scoria. For every Si atom, there are two atoms of Mg or Fe and four atoms of oxygen. The highest and lowest Mg end-members are Mg_2SiO_4 and $Fe(II)_2SiO_4$, respectively. Panels (d), (e), and (f) of Fig. 2.4 show the chemical compositions of the olivine members with the maximum, intermediate, and minimum number of Mg atoms, respectively, from among the 115 analytical data for the Earth presented in Deer et al. (1997a), who reviewed the mineralogical properties of olivine. Huang (1989) detailed the structural properties, natural occurrences, equilibrium environment, and physicochemical properties of olivine in soil.

The olivine particles shown in panels (a) and (b) of Fig. 2.4 were picked by tweezers from the 0.5–0.2 mm fraction of the 2A1 horizon of the pedon shown in Fig. 4.5a. The EDX spectrum in Fig. 2.4c is similar to that of Fig. 2.4e, suggesting that this example has a composition close to the intermediate chemical composition of olivine. The powder XRD pattern (Fig. 2.4g) approximates the reference pattern (Fig. 2.4h, from Brindley and Brown 1980).

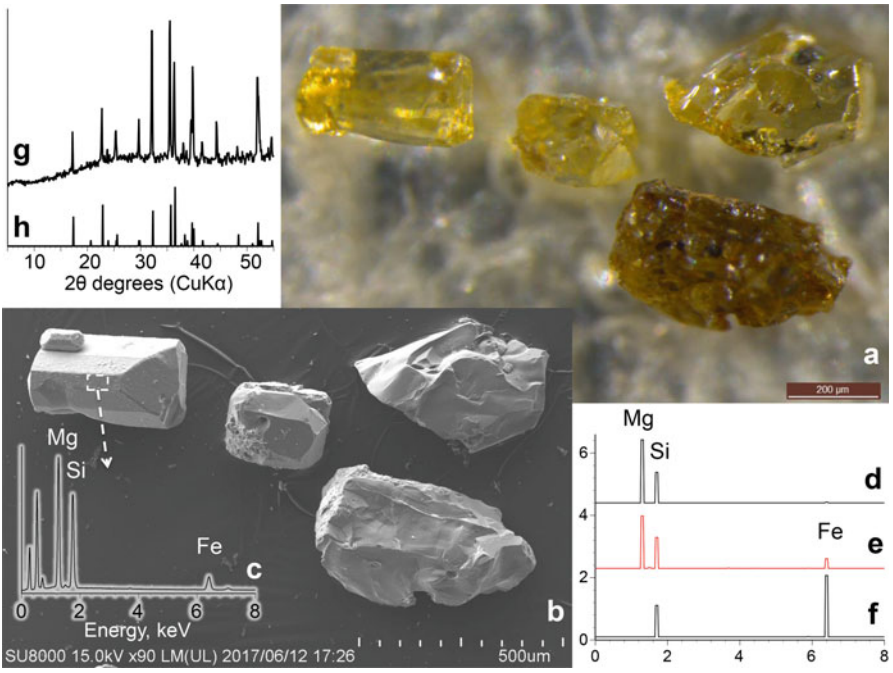

Fig. 2.4 Olivine particles from a scoria deposit from Mt. Fuji. (**a**) Optical photograph, (**b**) SEM image, (**c**) EDX spectrum. (**d**, **e**, and **f**) the elemental compositions of the olivine group minerals having the maximum, intermediate, and minimum number of Mg atoms, respectively, shown to mimic EDX spectra, (**g**) the powder XRD pattern of the olivine particles, (**h**) the reference powder XRD pattern (Brindley and Brown 1980). These olivine samples were separated from the soil profile shown in Fig. 4.5a

Pyroxene

Pyroxenes are single chain silicates that are linked laterally by cations such as Mg, Fe, Ca, and others. Pyroxenes are grouped by their chemical compositions into Mg–Fe pyroxene, Ca pyroxene, Na pyroxene, and others. Pyroxenes are also grouped into orthopyroxenes and clinopyroxenes according to their crystal system. As major pyroxenes, Mg–Fe pyroxene (enstatite–ferrosilite) of the orthopyroxenes and augite of the clinopyroxenes are introduced. According to its grouping by chemical composition, augite is one of the Ca pyroxenes. Deer et al. (1997b, 2013) described details of the pyroxenes.

Panels (f), (g), and (h) of Fig. 2.5 show the chemical compositions of the orthopyroxene members having the maximum, intermediate, and minimum number of Mg atoms, respectively, from among the 73 examples listed by Deer et al. (1997b). The vertical axis shows the number of cations per 6 oxygens. The maximum Mg member contains a small number of Fe atoms. The minimum Mg member contains a large number of Fe atoms and a small number of Ca atoms. The example shown in Fig. 2.5c corresponds to an orthopyroxene member between that of Fig. 2.5f and that of Fig. 2.5g. The powder X-ray diffraction pattern of the orthopyroxene sample is close to the reference, 31–634 (Hypersthene) of Joint committee on powder diffraction standards (1986).

The orthopyroxene shown in Fig. 2.5c was separated from the 2–0.25 mm fraction of the Tarumae-a (Ta-a) tephra sampled at Oiwake (Iburi Subprefecture, Hokkaido, Japan) (Mizuno et al. 2008) near the pedon site shown in Fig. 2.5a. The Ta-a tephra, erupted in 1739 from Mt. Tarumae, corresponds to the C horizon labeled as H5–2 of the soil profile shown in Fig. 2.5a. The soil color of the H5–2 horizon is whitish and the soil texture is sand, indicating that weathering is weak. Figure 2.5b shows not only light brown orthopyroxene but also light green augite, beige pumice-like volcanic glass, whitish feldspar, and some other grains from the tephra. Many of the crystalline minerals are partly or almost wholly covered with colorless volcanic glass.

Figure 2.6a shows augite, one of the clinopyroxenes, separated from the same fraction of the Ta-a tephra as the above-mentioned orthopyroxene. The color of the augite is light-green, and the grains are partly covered with colorless volcanic glass. The EDX spectra-mimic graphs Fig. 2.6d–f show the number of cations per 6 oxygen atoms of the augite members having the maximum, intermediate, and minimum number of Mg atoms, respectively, from among the 101 samples shown by Deer et al. (1997b). With a decrease in the Mg concentration, the concentration of Fe tends to increase. The number of Ca ions does not change very much compared with those of Mg and Fe among these members. The EDX spectrum (Fig. 2.6c) is close to Fig. 2.6e.

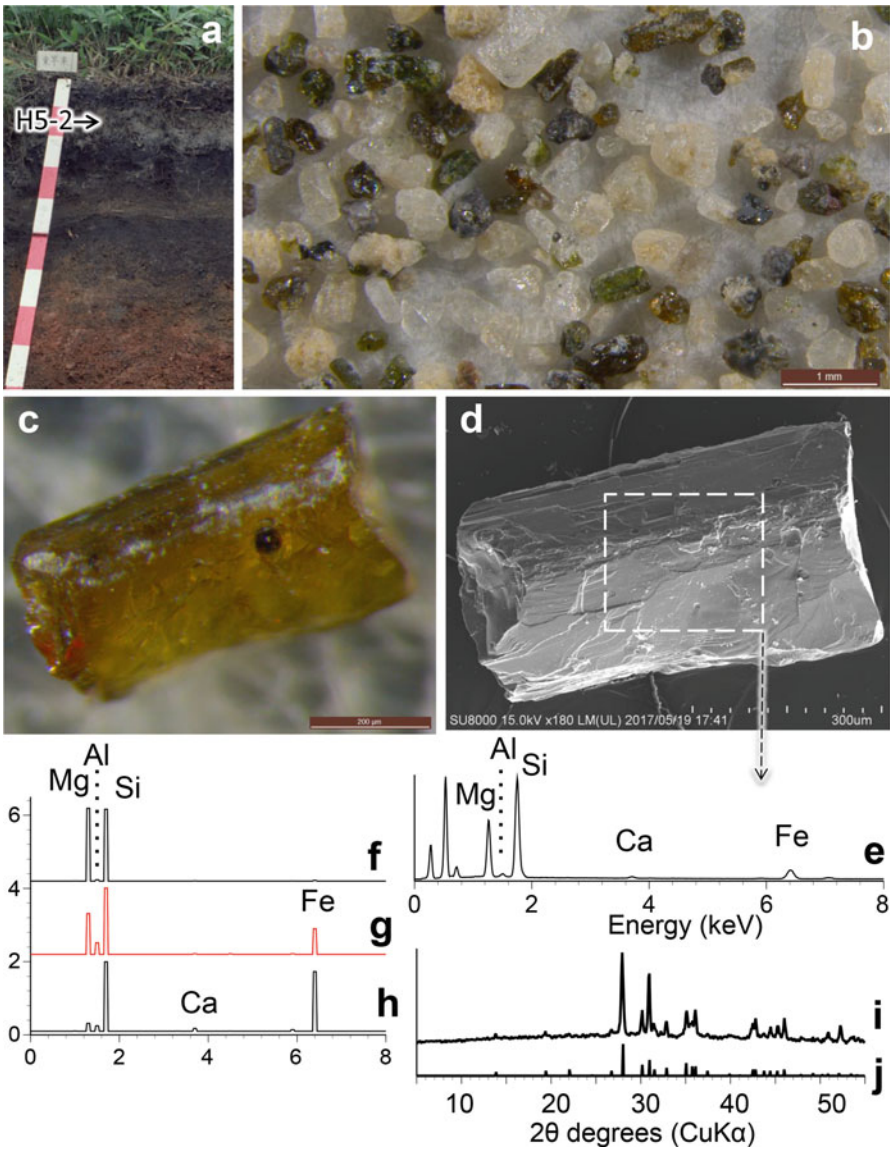

Fig. 2.5 Orthopyroxene of the Tarumae-a (Ta-a) tephra. (**a**) Ta-a tephra labeled as H5–2 in the soil profile, (**b**) optical micrograph of the 2–0.25 mm fraction separated from the Ta-a tephra, (**c** and **d**) optical micrograph and SEM image of an orthopyroxene particle, respectively, (**e**) EDX spectrum of the dashed area of (**d**), (**f**, **g**, and **h**) EDX spectra-mimic graphs showing the elemental compositions of orthopyroxenes with the maximum, intermediate, and minimum number of Mg atoms (Deer et al. 1997b), (**i** and **j**) powder XRD pattern of the orthopyroxene particles and reference powder XRD pattern, respectively (Joint committee on powder diffraction standards 1986)

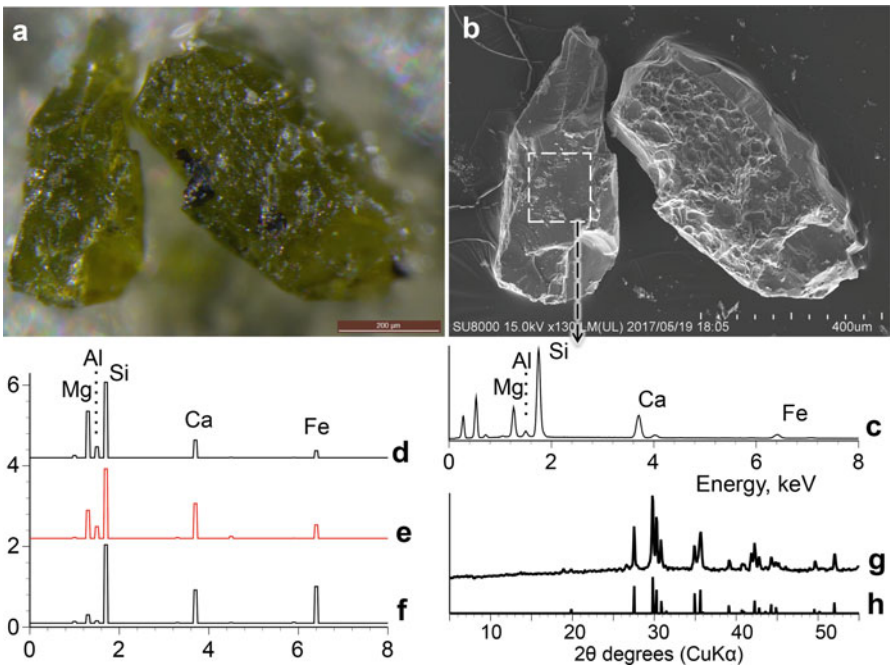

Fig. 2.6 Augite separated from the Ta-a tephra. (**a**) Optical micrograph, (**b**) SEM image of the augite, (**c**): EDX spectrum of the dashed area in (**b**), (**d**, **e**, and **f**) elemental compositions of augites with the maximum, intermediate, and minimum number of Mg ions, respectively (Deer et al. 1997b). (**g**) Powder XRD pattern of the augite particles, (**h**) reference powder XRD pattern (24-203 of Joint committee on powder diffraction standards 1986)

Amphibole

Amphiboles are double chain silicates (Table 2.1). Between the double chains, several cations link the double chain silicates. The general chemical composition is formulated as follows:

$A_{0\text{-}1}B_2C_5T_8O_{22}(OH)_2$

For example, in the Ca-rich amphiboles,
A: Na, K, or vacant
B: Ca, Na, Mn
C: Mg, Fe^{2+}, Fe^{3+}, Al, Ti, Mn, Cr or other
T: Si, Al

The cations at the A, B, C, and T sites play their own roles. The C site cations are sandwiched with two double chain silicates. The sandwiched double chain silicates are laterally linked by the B site cations. The OH group, which is bound to C site cations, can be partially or wholly replaced by F and Cl. In the case of oxyhornblende, the OH group is replaced by oxygen. The T site is the silicate chain.

Depending on the B-site cations, amphiboles are grouped as calcic amphibole, sodic amphibole, sodic-calcic amphibole, and iron-magnesium-manganese amphibole. Hornblendes, commonly found amphiboles, are grouped as calcic amphibole and are members of the magnesio-hornblendes (Mg can be replaced by Fe^{2+} in a wide range) at the lower level of grouping (Deer et al. 1997c).

Hornblendes often occur in volcanic ash. Figure 2.7a, b show dacitic volcanic ash erupted from Mt. Pinatubo (Zambales Mountains, Philippines) in June 1991 (Wolfe and Hoblitt 1996) and re-deposited along large rivers as lahar (mudflow) deposits. In the 0.2–0.5 mm fraction (Fig. 2.7c), hornblendes can be seen as black prismatic particles in a mixture of sponge-like volcanic glass, feldspars, quartz, etc.

The black prismatic particle appears dark-greenish under an optical microscope (Fig. 2.8a). The EDX spectrum (Fig. 2.8c) indicates that Na, Mg, Al, Si, Ca, and Fe are contained in the particle. The EDX spectrum-mimic graphs (Fig. 2.8d–f) show the number of cations per 23 oxygens or 24 (O, OH, F) of the maximum, intermediate, and minimum Mg members from 206 hornblende group minerals listed by Deer et al. (1997c). With decreasing number of Mg atoms, the number of Fe atoms tends to increase. The number of Ca atoms does not vary as much as those of Mg and Fe. The EDX spectrum of Fig. 2.8c corresponds to a member between those of Fig. 2.8d and e. Although the elemental composition of hornblende may be similar to that of augite (Fig. 2.6), the morphological properties, color, and XRD pattern of

Fig. 2.7 Lahar deposit from Mt. Pinatubo, Philippines. (**a**) Landscape of the lahar deposit at the Pasig-Potrero River, (**b**) profile of the lahar deposit, (**c**) an optical micrograph of the 0.2–0.5 mm fraction of the lahar deposit

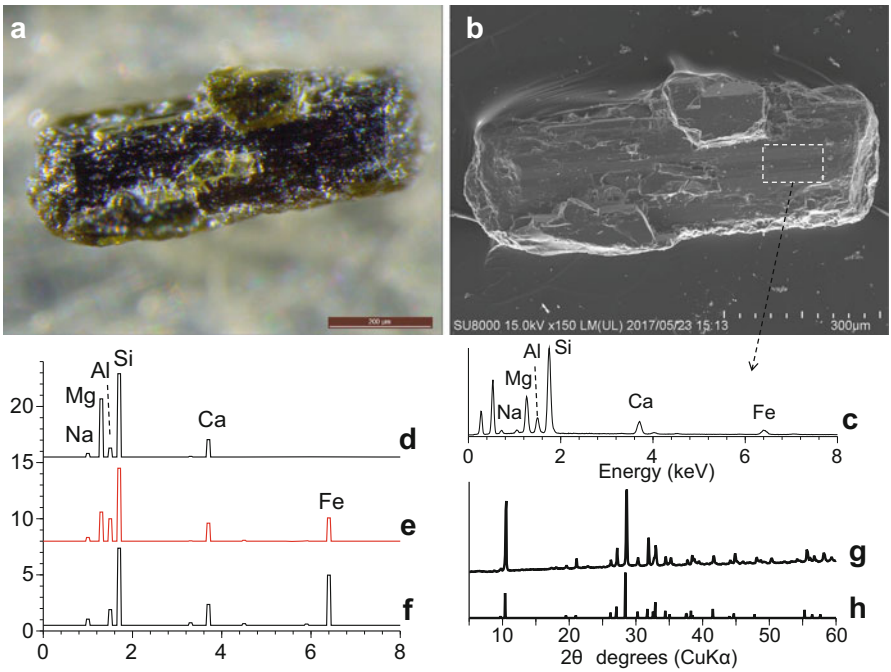

Fig. 2.8 Hornblende particle from the 0.2–0.5 mm fraction of the 1991 Pinatubo tephra taken from the 1992 lahar deposit (Fig. 2.7). (**a**) Optical micrograph, (**b**) SEM image, (**c**) EDX spectrum of the dashed area in (**b**), (**d**, **e**, and **f**) EDX spectrum-mimic graphs showing the elemental compositions of the maximum, intermediate, and minimum Mg members of hornblende, respectively (Deer et al. 1997c), (**g**) powder XRD pattern of the hornblende particles, (**h**) reference powder XRD pattern of hornblende (Joint committee on powder diffraction standards 1986)

hornblende are different from those of augite. The XRD pattern (Fig. 2.8g) resembles 21–149 (Magnesio-hornblende, ferroan) of Joint committee on powder diffraction standards (1986) (Fig. 2.8h).

Micas

Micas are phyllosilicates, which have basal cleavage and flat shape. Micas are one of the major components of igneous, sedimentary, and metamorphic rocks. Abundant members of the micaceous primary minerals are the muscovite and biotite series minerals. The structures of micas are introduced in Chap. 3 with those of other phyllosilicate minerals.

Muscovite

Muscovite (dioctahedral mica) is colorless, transparent, and more resistant to weathering than biotite, a trioctahedral mica. Figure 2.9c shows minerals in the coarse sand fraction separated from a granitic soil in the Republic of Korea. The colorless, transparent, and flat particles are muscovite. As shown in Fig. 2.10a (optical micrograph) and (b) (SEM image), the surface of the muscovite is highly flat, smooth, and appears mostly un-weathered. In contrast, the brown and partly shiny particles appear to be weathered biotite particles in Fig. 2.9c.

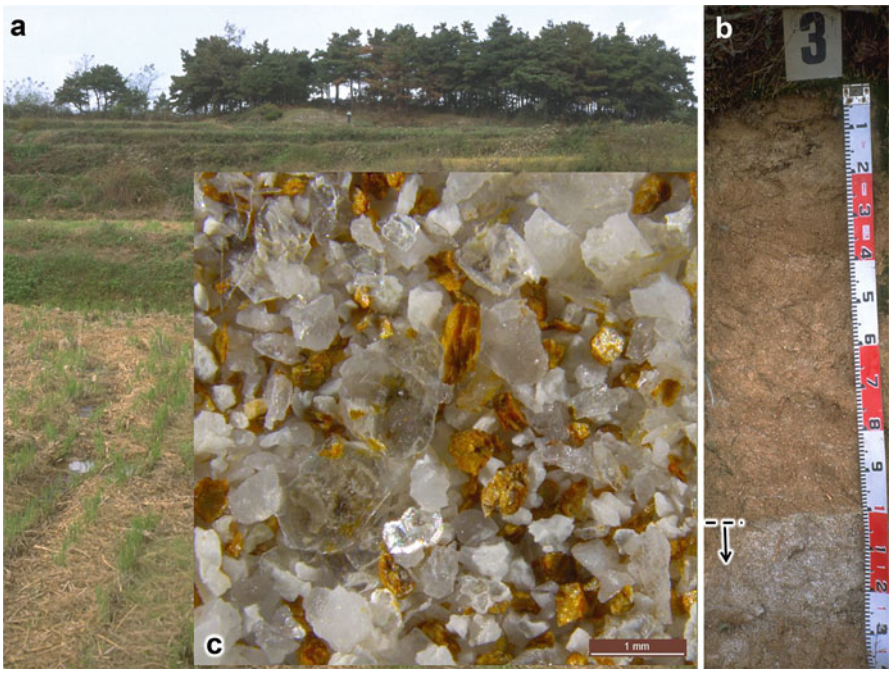

Fig. 2.9 Granitic soil in Singun-ri, the Republic of Korea. (**a**) Landscape, (**b**) soil profile and (**c**) 2–0.2 mm fraction of the soil. The 2–0.2 mm fraction of the C horizon (indicated by an arrow in (**b**), 100–125+ cm from the surface) includes feldspar, quartz, white mica, weathered biotite, and other minerals

The aluminum concentration of muscovite is relatively high among the primary minerals. The EDX spectrum-mimic graphs, Fig. 2.10d–f, show the number of cations for the maximum, intermediate, and minimum Al members, respectively, from among 70 muscovites, phengites, and other potassic white micas per 12 (O, OH, F) or 22 anions (Fleet 2003). The number of Al ions in Fig. 2.10d, e is close to that of Si. According to the ideal chemical formula for muscovite (Table 2.1), the number of Al atoms is the same as the number of Si atoms. In phengite, a portion of the Al at the octahedral sites is replaced by Mg^{2+}. The minimum Al member, Fig. 2.10f, is celadonite, in which isomorphous substitution at the octahedral sites is small and the octahedral sites are occupied by Fe^{3+} and Mg^{2+}. The powder XRD pattern, Fig. 2.10g, is close to the reference pattern for muscovite, Fig. 2.10h.

Biotite

The biotite series comprises trioctahedral micas with compositions between, or close to, the phlogopite–annite and eastonite–siderophyllite joins, and also includes tetraferriphlogopite and tetraferriannite because biotite often contains small amounts of Fe^{3+} in its tetrahedral sites (Fleet 2003). Figure 2.11 shows an example of a relatively un-weathered biotite particle from a mudflow deposit of Mt. Pinatubo, Philippines (Fig. 2.7), although biotite particles are not particularly abundant in the mudflow deposit. The shape of the particle is hexagonal and platy. The EDX

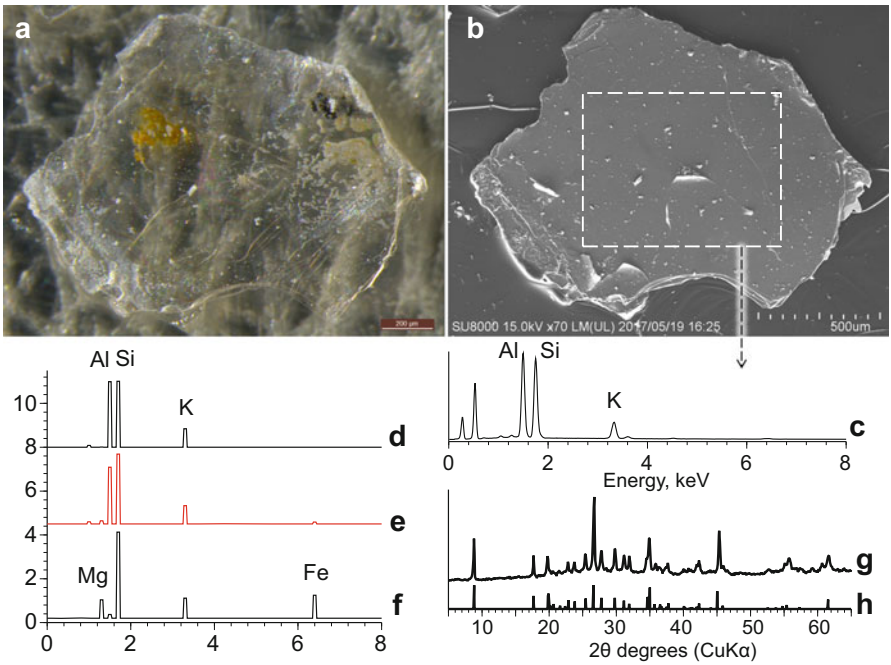

Fig. 2.10 White mica from Singun-ri, the Republic of Korea. (**a**) Optical micrograph, (**b**) SEM image, (**c**) EDX spectrum of the dashed area in (**b**), (**d**, **e**, and **f**) EDX spectrum-mimic graphs showing the elemental compositions of the maximum, intermediate, and minimum Al members of muscovite, respectively, (**g**) powder XRD pattern of the muscovite particles, (**h**) reference powder XRD pattern (Brindley and Brown 1980)

spectrum (Fig. 2.11c) suggests that the chemical composition is between those of the maximum and intermediate Mg members. Although the color is close to black, the chemical composition is not uniform. Partial weathering might have already started because a portion of the K^+ was exchanged with Ca^{2+} during transportation from the original site of deposition by rain and river water.

According to quantitative analyses of several particles similar to the one in Fig. 2.11a, the Mg/(Mg + Fe) atomic ratio ranges between 60 and 70%, indicating that these particles are a Mg-biotite close to phlogopite (Nanzyo et al. 1999). The powder XRD pattern (Fig. 2.11g) is close to that for phlogopite (1 M), Fig. 2.11h (Brindley and Brown 1980).

Further readings for micas are Funning et al. (1989), Thompson and Ukarainczyk (2002).

Feldspars

Feldspars, including plagioclase and alkali feldspar, account for half of the minerals of the Earth's crust (Fig. 2.1). Feldspars are tectosilicates (Table 2.1) and their three end-members are orthoclase, albite, and anorthite (Fig. 2.12). Depending on their formation temperature, feldspars are divided into high- and low-temperature types (Dear et al. 2013). The dotted area of the triangle (Fig. 2.12) shows elemental

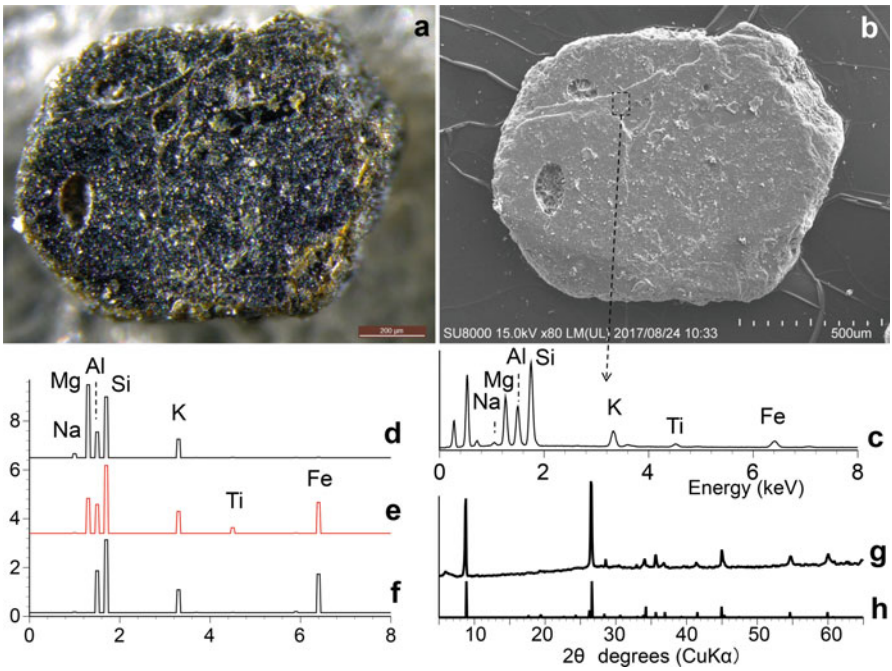

Fig. 2.11 Biotite from a lahar deposit of Mt. Pinatubo. (**a**) Optical micrograph, (**b**) SEM image, (**c**) EDX spectrum of the dashed area in (**b**), (**d**, **e**, and **f**) EDX spectrum-mimic graphs showing the elemental compositions of the maximum, intermediate, and minimum Mg members of the biotite series (112 samples) listed by Fleet (2003), (**g**) powder XRD pattern of the biotite particles, (**h**) reference powder XRD pattern (Brindley and Brown 1980)

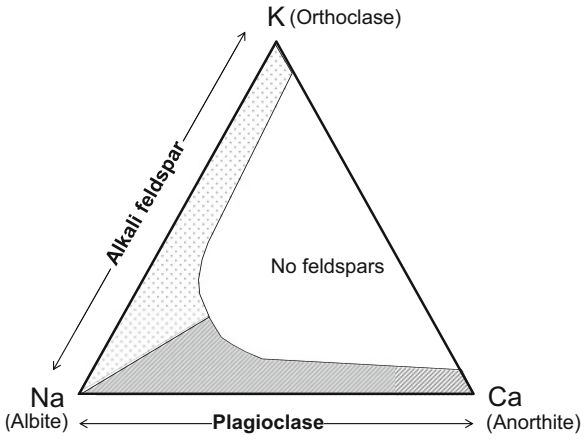

Fig. 2.12 Simplified triangle diagram showing the K, Na, and Ca compositions of natural feldspars and their end-members (orthoclase, albite, and anorthite)

compositions of the alkali feldspars. With slow cooling, the alkali feldspars tend to convert to the two areas near orthoclase and albite. Plagioclase (shaded area of Fig. 2.12) is regarded as a solid solution of two end members, albite and anorthite, and is divided into four general categories. These are oligoclase (Albite: 90–70%), andesine (Albite: 70–50%), labradorite (Albite: 50–30%), and bytownite (Albite: 30–10%). No feldspar exists in the white area. When high-temperature feldspars are cooled rapidly, they may retain the high-temperature phase at ambient temperature. The low-temperature type occurs in the plutonic rock that cools slowly at deeper sites. Feldspars are often colorless but are generally less transparent than quartz. Feldspars in soil tend to have various shapes with broken edges and some parallel cleavage surfaces within or bounding the particles.

Figure 2.13a, b show an example of a nearly un-weathered plagioclase collected from a lahar deposit from the 1991 Mt. Pinatubo eruption. In the optical micrograph (Fig. 2.13a), parallel cleavage planes can be observed weakly within the particle.

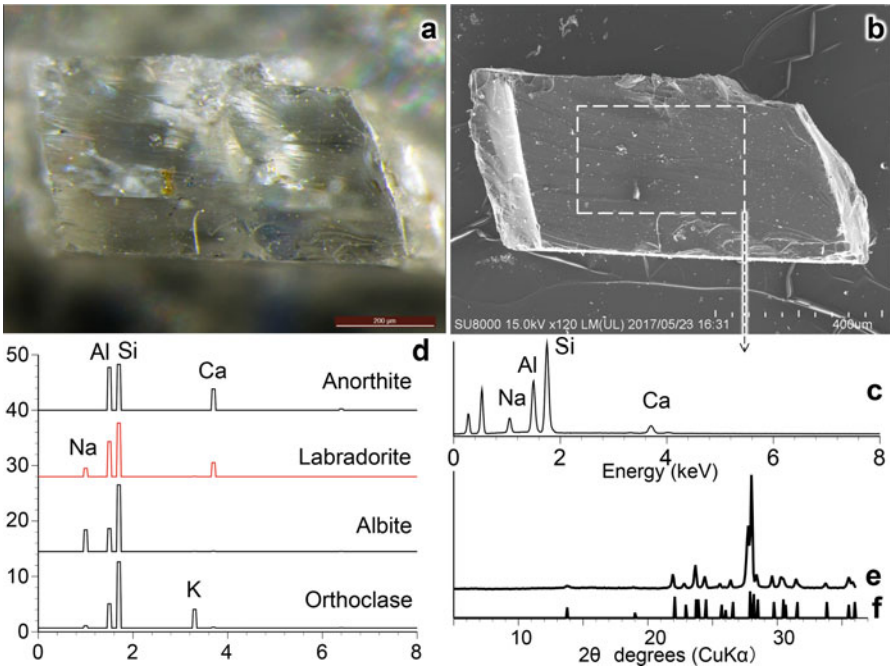

Fig. 2.13 A feldspar particle from the Mt. Pinatubo lahar deposit (1991). (**a**) Optical micrograph, (**b**) SEM image, (**c**) EDX spectrum of the dashed area in (**b**), (**d**) elemental compositions of the members having the intermediate number of Ca atoms among the 7 anorthites, the intermediate number of Ca atoms among the 10 labradorites, the intermediate number of Na atoms among the 10 albites, and the intermediate number of K atoms among the 62 K-feldspars listed by Deer et al. (2001). The powder XRD pattern of the hand-picked feldspar particles (**e**) is close to that of the natural labradorite (**f**) reported by Goodyear and Duffin (1955). The latter powder XRD pattern was obtained as a diffraction photograph, and the peak heights represent relative intensities that were estimated visually

The EDX spectrum-mimic graphs (Fig. 2.13d) show the number of cations per 32 oxygens. Four representatives were chosen from among the 7 anorthites, 10 labradorites, 10 albites, and 62 K-feldspars (sanidine, orthoclase, microcline, amazonite, etc.) listed by Deer et al. (2001). Referring to Fig. 2.13d, the EDX spectrum shown in Fig. 2.13c is close to that of labradorite, one of the plagioclase feldspars.

Plagioclase also exists as high- and low-temperature phases. The high- and low-temperature types of albite and oligoclase can be identified from a powder XRD pattern, but it gradually becomes difficult with a further increase in the ratio of anorthite (Huang 1989). The powder XRD pattern (Fig. 2.13e) appears closer to, although not completely the same as, the pattern of natural labradorite listed as No. 6 by Goodyear and Duffin (1955), low-temperature labradorite, than to the synthetic one, high-temperature type.

2.3.2.2 Silica Minerals

Among the various silica minerals in soils are quartz and cristobalite, which are grouped as tectosilicates (Table 2.1) (Drees et al. 1989; Deer et al. 2004). Mizota and Aomine (1975) reported cristobalite in the clay fraction of volcanic ash from Hokkaido, Japan.

Quartz, in particular, is found in the silt and sand fractions of many soils, although clay-sized quartz does exist in some soils affected by airborne dust. Quartz grains are colorless and transparent in many cases. There are two structure types, high- and low-temperature types, distinguishable by their XRD patterns (Brindley and Brown 1980), and the one in soils is the low-temperature type. Cracks sometimes can be found in quartz grains, possibly due to shrinkage as they cooled and converted from the high-temperature type to the low-temperature type. Conchoidal fractures are also a characteristic of quartz grains. Surface etchings due to partial dissolution are very slight.

Figure 2.14a (optical micrograph) and (b) (SEM image) show a colorless and transparent quartz grain separated from a volcanic ash deposit (1991) remobilized in a lahar from Mt. Pinatubo (Fig. 2.7). A conchoidal fracture can be observed on the left side (Fig. 2.14b). As is often the case of minerals in volcanic ash, the quartz grain is partly covered by volcanic glass. The EDX spectrum of the exposed quartz surface shows only Si (Fig. 2.14c). The powder XRD pattern (Fig. 2.14d) of a hand-picked quartz grain from the volcanic ash is identical to that of the low-temperature type of quartz (Fig. 2.14e) (Brindley and Brown 1980), although a very small reflection peak at about $2\theta = 28$ degrees, probably from plagioclase, is included in Fig. 2.14d.

All the quartz in soil is the low-temperature phase because inter-conversion between high- and low-temperature quartz occurs rapidly. The powder XRD pattern for high-temperature quartz is different from that of low-temperature quartz.

Further readings for silica minerals are Drees et al. (1989), Monger and Kelly (2002) and Deer et al. (2004).

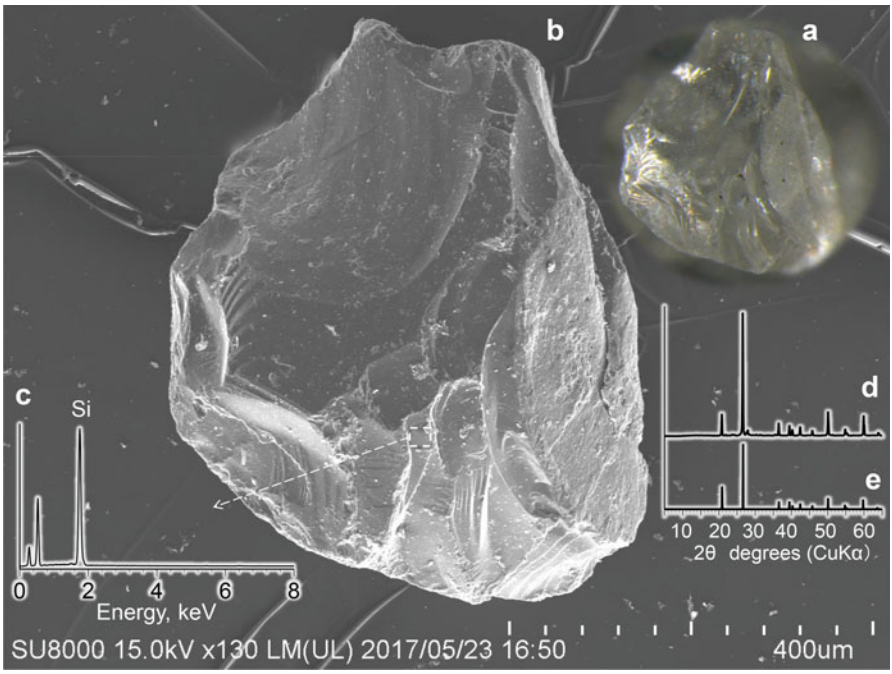

Fig. 2.14 Quartz from the 0.2–0.5 mm fraction of the 1991 Pinatubo tephra taken from the lahar deposit (Fig. 2.7). (**a**) Optical micrograph, (**b**) SEM image, (**c**) EDX spectrum acquired from the dashed area shown in (**b**), (**d**) powder XRD pattern of quartz grains, (**e**) reference powder XRD pattern (Brindley and Brown 1980)

2.4 Other Minerals in Soil

2.4.1 Titanomagnetite and Ilmenite

Iron-titanium (Fe-Ti) oxides are accessary minerals in many soils. The Fe-Ti oxides include magnetite [Fe_3O_4], titanomagnetite [$(1\text{-}x)Fe_3O_4.xFe_2TiO_4$] and ilmenite [$FeTiO_3$] (Allen and Hajek 1989; Milnes and Fitzpatrick 1989). Chemical compositions of these oxides are conveniently displayed on the TiO_2-FeO-$1/2Fe_2O_3$ ternary diagram (Butler 1992).

Figure 2.15a is an optical micrograph of magnetite particles collected from the lahar deposit from Mt. Pinatubo (Fig. 2.7) using a hand magnet, suggesting that these particles are rich in titanomagnetite. Titanomagnetite has dark color and is not transparent. Figure 2.15b is the SEM image of the dashed part of Fig. 2.15a, and the dashed square in Fig. 2.15b yielded the EDX spectrum shown in Fig. 2.15c, which suggests the elemental composition of ferrian ilmenite (Imai et al. 1996) or titanohematite (Butler 1992). An EDX spectrum with smaller amount of Ti, (Fig. 2.15d), was obtained from other part of the same particle lacking a glass coating. The powder XRD pattern of the crushed magnetic particles is shown as

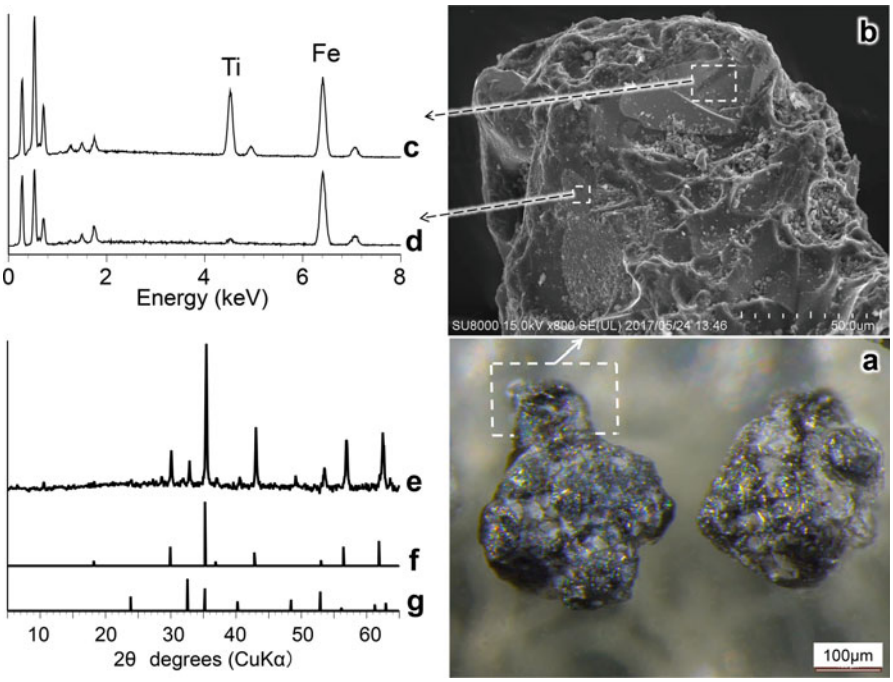

Fig. 2.15 Magnetic minerals collected from the Mt. Pinatubo lahar deposit (Fig. 2.7). (**a**) Optical micrograph, (**b**) magnified SEM image of the dashed area in (**a**), (**c** and **d**) EDX spectra of the dashed area in (**b**) and a magnetic particle with little Ti, respectively, (**e**) powder XRD pattern. Powder XRD patterns of titanomagnetite (Joint Committee on Powder Diffraction Standards No.75-1376) (**f**) and ilmenite (Brindley and Brown 1980) (**g**) are shown as references

Fig. 2.15e. It is evident that the major XRD pattern is similar to that of titanomagnetite (Joint Committee on Powder Diffraction Standards No. 75-1376) and that the XRD pattern close to ilmenite (Brindley and Brown 1980) is also included. It is frequently difficult to distinguish magnetite from titanomagnetite, and ilmenite from hematite using XRD because of their somewhat similar patterns (Milnes and Fitzpatrick 1989).

As titanomagnetite is soluble, at least partly, in oxalate solution, it affects the evaluation of Fe in soils when using oxalate extraction (Rhoten et al. 1981; Walker 1983; Shoji et al. 1987). Accordingly, in the requirements for Andisols (Soil Survey Staff 1999) and Andosols (IUSS Working Group WRB 2015), the phosphate retention percentage is used together with the oxalate extraction.

2.5 Mineral Samples in Soil Derived from a Weathered Granitic Rock

Relatively fresh or un-weathered primary minerals were introduced in the previous sections. However, the minerals in soil environments are physically and chemically altered to varying degrees under the activity of biota. In this section, a soil formed on

Cretaceous granitoids (Kon et al. 2015) is exemplified. The soil is located at the dam lakeshore of the Utsushi–Gawa River (Figs. 6.17 and 6.24), bottom of a valley slope in the central Abukuma Plateau, northeastern Japan Arc. Although the age of the bedrock is old, the soil developed at the bottom of the valley slope can be much younger than the bedrock due to subsequent continuous erosion. This soil is a shallow Udept with A, Bw, and C horizons under a bamboo forest (Fig. 2.16a, b). The 2–0.2 mm fraction of the Bw horizon includes quartz, feldspar, biotite, hornblende, and others showing different intensities of weathering (Fig. 2.16c).

Among the mineral particles in Fig. 2.16c, quartz has a high resistance to weathering. Figure 2.16d shows an optical micrograph of a particle that consists mostly of quartz. Although a crack occurs at the arrowed site of the SEM image (Fig. 2.16e), it may have formed by shrinkage during the phase transformation from high- to low-temperature quartz. Although conchoidal fractures, which are characteristic of quartz, are found on the surface (Fig. 2.16g), almost no etching due to weathering can be seen.

The feldspar particle in Fig. 2.17a has a whitish color and is not transparent. Similar particles can be found in Fig. 2.16c. According to the SEM image (Fig. 2.17b) and the magnified SEM image (Fig. 2.17c), surface etching and opening of cleavage planes are evident due to weathering.

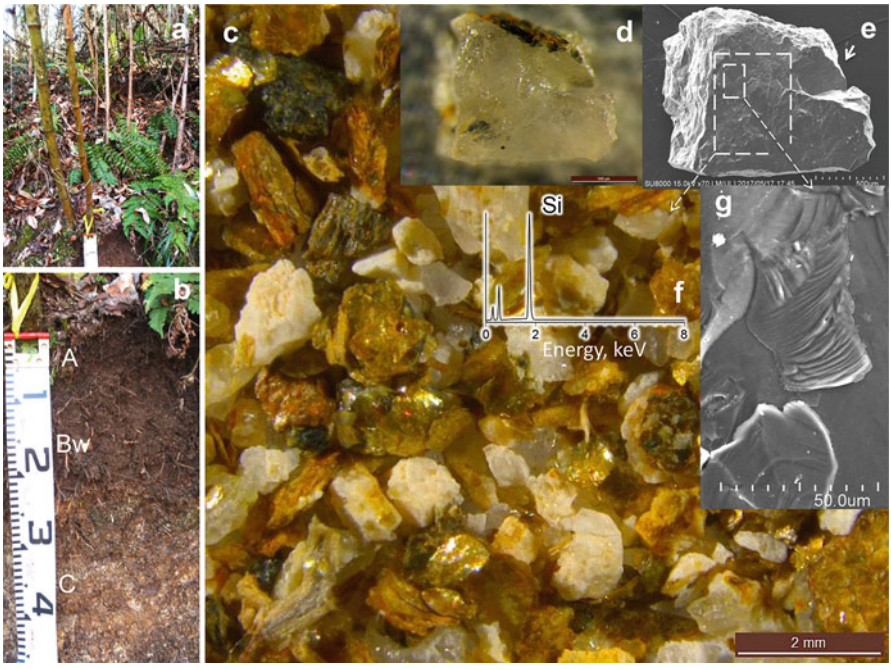

Fig. 2.16 Coarse sand fraction of the Bw horizon of soil sampled from the dam lakeshore of the Utsushi–Gawa River, Japan. (**a**) Vegetation, (**b**) soil profile, (**c**) 2–0.2 mm fraction of Bw horizon, (**d**) selected quartz particle, (**e**) SEM image of (**d**), (**f**) EDX spectrum obtained from the larger dashed area in (**e**), (**g**) magnified SEM image of the smaller dashed area indicated in (**e**)

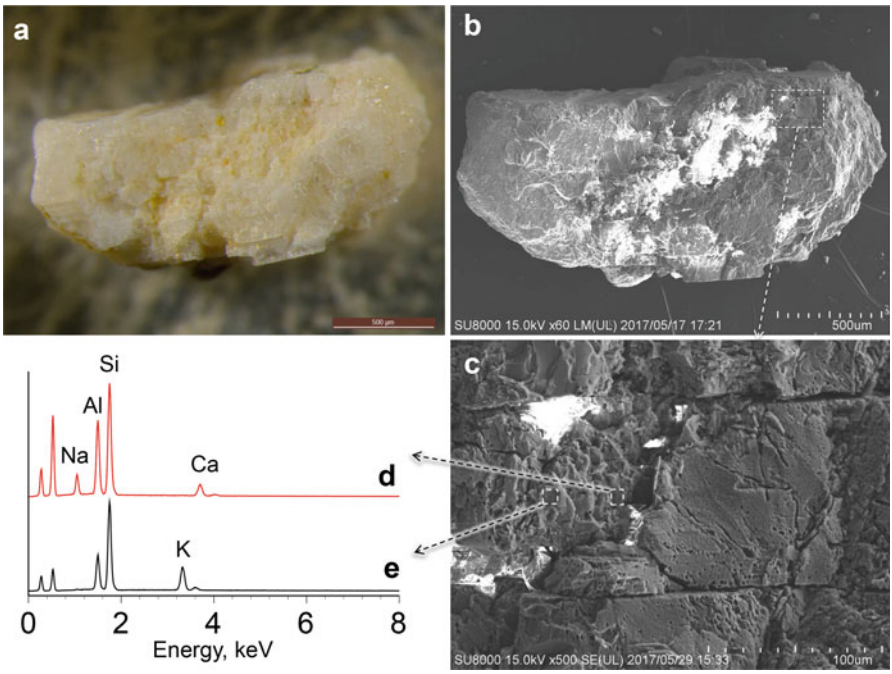

Fig. 2.17 Weathered feldspar from the 2–0.2 mm fraction (Fig. 2.16c). (**a**) Optical micrograph, (**b**) SEM image, (**c**) magnified SEM image of the dashed area in (**b**), (**d** and **e**) EDX spectra of the dashed areas in (**c**). The EDX spectra (**d**) and (**e**) suggest plagioclase and K-feldspar, respectively

Another property found in feldspar is complexity or microtexture. For example, two EDX spectra, (d) and (e), were obtained from the selected areas in Fig. 2.17c. The EDX spectra of Fig. 2.17d, e corresponds to those of plagioclase and orthoclase in Fig. 2.13d, respectively.

Using a polished section (Fig. 2.18a), the combination of different minerals and microtextures in a gravel particle can be observed clearly by using SEM-EDX. The polished section was prepared by embedding gravel particles in a resin and then cutting and polishing (see Sect. 1.4). The arrowed particle from Fig. 2.18a was selected. The optical micrograph (Fig. 2.18b) shows that this gravel particle has several different parts, weakly transparent, cloudy, and dark. Brown, fine-textured soil materials partly surround the gravel particle.

The element maps in Fig. 2.18 show that this gravel particle consists of several different minerals, more than are apparent from the optical micrograph (Fig. 2.18b). Looking at the Si element map, there are more than three levels of different Si concentration areas, suggesting different minerals. From these element maps, at least six different mineral areas can be identified, as listed below (numbered in the Si map of Fig. 2.18):

(1) An area with high Mg and Fe concentrations and medium Ca concentration.
(2) Areas with the highest Si concentration and near-zero concentrations of other elements.

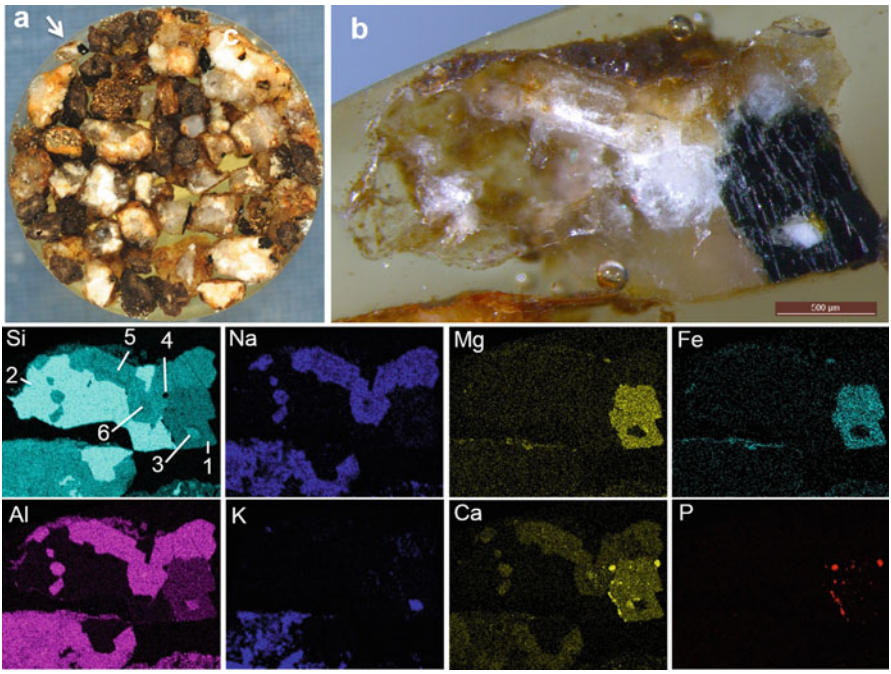

Fig. 2.18 Gravel particles of the Bw horizon (Fig. 2.16b). (**a**) Polished section, (**b**) optical micrograph of the particle arrowed in (**a**), and element maps of Si, Al, Na, K, Mg, Ca, Fe, and P obtained by SEM-EDX

(3) Areas with high K concentration and almost no Na and Ca atoms.
(4) Areas with the highest Ca and P concentrations.
(5) Areas with high Na and Al concentrations and low Ca concentration.
(6) A small area with the highest Al concentration, near-zero Na and K concentrations, and medium Ca concentration.

The three EDX spectra (Fig. 2.19b–d) represent the areas (b), (c), and (d), respectively, shown in Fig. 2.19a. A comparison of the EDX spectra shown in Sects. 2.3 and 2.4 with those of Fig. 2.19b–d suggest hornblende (the area (1)), quartz (the areas (2)), and K-feldspar (the areas (3)), respectively. The areas (4) correspond to apatite, which is discussed in Sect. 6.3.

The small area (6) of Fig. 2.18, also selected as Fig. 2.19e, shows the highest Al concentration, almost no Na, no K, and a medium-level concentration of Ca. A further complex pattern can be observed in the magnified SEM image (Fig. 2.20). The EDX spectrum obtained from the small area having medium Ca concentration (Fig. 2.20b) suggests anorthite (Fig. 2.13d). The areas around the anorthite are close to Na-rich plagioclase, or oligoclase (the areas (5)) (Fig. 2.20a). When solid solutions of high-temperature feldspars cool, they tend to separate into their end-members and form a complex microtexture of the end-members (Huang 1989).

Thus, the gravel particle resembles a rock fragment having complex minerals. Furthermore, the microtextures of the feldspars might have resulted from the

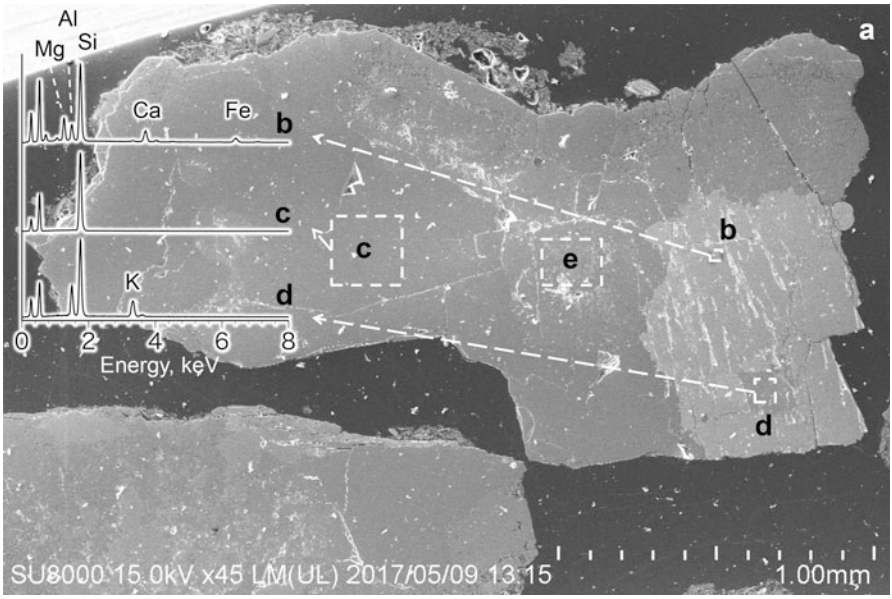

Fig. 2.19 Polished section of a gravel particle (Fig. 2.18b). (**a**) SEM image, (**b**, **c**, and **d**) EDX spectra of the dashed areas (**b**), (**c**), and (**d**), respectively. The dashed area (**e**) includes a relatively high Ca area

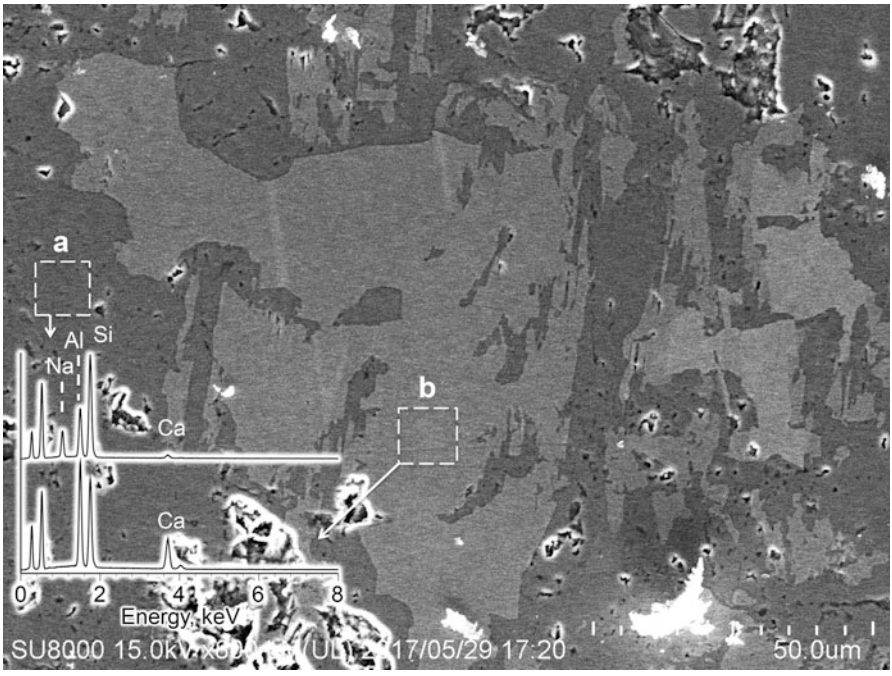

Fig. 2.20 Magnified SEM image of Fig. 2.19e and EDX spectra (**a** and **b**) of dashed areas **a** and **b**, respectively

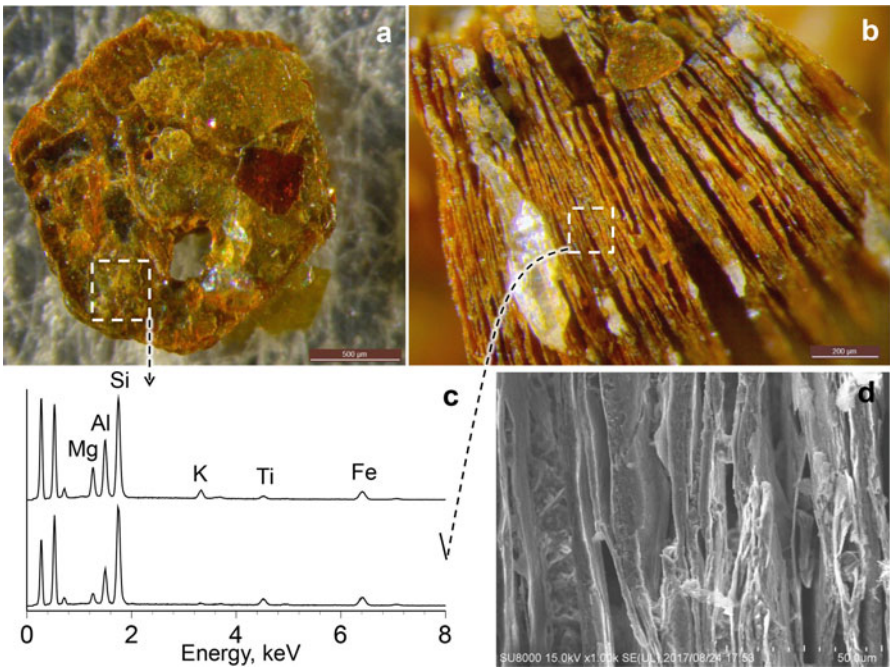

Fig. 2.21 A weathered biotite particle separated from the 2–0.2 mm fraction (Fig. 2.16c). (**a** and **b**) Optical micrographs of a plane site and an edge site, respectively, (**c**) EDX spectra of the selected areas in (**a**) and (**b**), (**d**) magnified SEM image of the edge site of (**b**)

conversion of high- to low-temperature phases during the cooling process. A single feldspar particle can be composed of different feldspars, as suggested by Fig. 2.17c.

Biotites tend to weather much more easily than muscovite and many other minerals. The coarse fraction (2–0.2 mm) exemplified in Fig. 2.9c includes many weathered biotite particles, as well as muscovite particles that show only weak weathering. The coarse sand fraction of Fig. 2.16c also contains many weathered biotite particles. Weathered biotite in soil shows mostly brown or golden colors, although the hexagonal platy properties of the mineral may partly or wholly remain (Fig. 2.21a). The originally flat cleavage face becomes wavy, and the edges of the particle exfoliate along cleavage (Fig. 2.21b, d). The remaining K is distributed non-uniformly (see EDX spectra in Fig. 2.21c). Hydrobiotite, vermiculite, and halloysite have been detected in weathered biotite particles (Masui 1954).

Hornblende particles also occur in the sand fraction (Fig. 2.16c). Although the hornblende particles maintain their prismatic appearance, they are easily broken into finer fragments when handled by tweezers, indicating that they are also partly weathered.

The weathering intensity of the primary minerals in the sand fraction of the exemplified granitic soil is variable depending on the mineral species. Further variation may be added by climatic conditions, redox conditions, age of the soil, and other environmental factors. Thus, partially weathered sand-size minerals may exchange or

fix ions. As will be shown in Sect. 6.2, weathered biotite particles in the sand fraction fix radiocesium. Other possible functions supporting plant growth are the release and tentative retention of nutrient elements, water, etc., although the capacity of these functions of the coarse fraction is not as high as that of clays and humus.

Further readings are Huang (1989) and Deer et al. (2013)

References

Allen BL, Hajek BF (1989) Mineral occurrence in soil environments. In: Dixon JB, Weed SB (eds) (Co-eds) minerals in soil environments, 2nd edn. Soil Science Society of America, Madison, pp 199–278

Brindley GW, Brown G (1980) Crystal structures of clay minerals and their X-ray indentification. Mineralogical society monograph no.5. Mineralogical Society, London

Butler RF (1992) Ferromagnetic minerals. In: Paleomagnetism: Magnetic domains to geologic terranes, Blackwell Scientific Publications, pp16–30

Deer WA, Howie RA, Zussman J (1997a) Rock-forming minerals, Orthosilicates, 2nd edn. The geological society, London

Deer WA, Howie RA, Zussman J (1997b) Rock-forming minerals, single-chain silicates, 2rd edn. The geological society, London

Deer WA, Howie RA, Zussman J (1997c) Rock-forming minerals, double-chain silicates, 2rd edn. The geological society, London

Deer WA, Howie RA, Zussman J (2001) Rock-forming minerals, framework silicates: feldspars, 2nd edn. The geological society, London

Deer WA, Howie RA, Zussman J (2004) Rock-forming minerals, framework silicates: silica minerals, feldspathoids and the zeolites, 2nd edn. The geological society, London

Deer WA, Howie RA, Zussman J (2013) An introduction to the rock-forming minerals, 3rd edn. Mineralogical society, London

Drees LR, Wilding LP, Smeck NE, Senkayi AL (1989) Silica in soils: quartz and disordered silica polymers. In: Dixon JB, Weed SB (eds) (Co-eds) minerals in soil environments, 2nd edn. Soil Science Society of America, Madison, pp 913–974

Fanning DS, Keramidas VZ, El-Desoky MA (1989) Micas. In: Dixon JB, Weed SB (eds) (Co-eds) minerals in soil environments, 2nd edn. Soil Science Society of America, Madison, pp 551–634

Fleet ME (2003) Rock-forming minerals, micas, 2nd edn. The geological society, London

Glossary of Soil Science Terms Committee (2008) Glossary of soil science terms. Soil Science Society of America, Inc, Madison

Goodyear J, Duffin WJ (1955) The identification and determination of plagioclase feldspars by the X-ray powder method. Miner Mag J Miner Soc 30:306–326

Huang PM (1989) Feldspars, olivines, pyroxenes, and amphiboles. In: Dixon JB, Weed SB (eds) (Co-eds) minerals in soil environments, 2nd edn. Soil Science Society of America, Madison, pp 975–1050

Imai A, Listanco EL, Fujii T (1996) Highly oxidized and sulfur-rich dacitic magma of Mount Pinatubo: Implication for metallogenesis of porphyry copper mineralization in the western Luzon arc. In: CG Newhall and RS Punongbayan (eds) Fire and mud, Eruptions and lahars of Mount Pinatubo, Philippines, Philippine Institute of Volcanology and Seismology, Quezon city, University of Washington Press, Seattle and London, pp 865–874

IUSS Working Group WRB (2015) World reference base for soil resources 2014. International soil classification system for naming soils and creating lengends for soil maps, update 2015, World soil resources reports no.106. FAO, Rome

Joint Committee on Powder Diffraction Standards (1986) Mineral powder diffraction file: data book. International Center for Diffraction Data, Swarthmore

Kon Y, Morita S, Takagi T (2015) Spatial U-Pb age distribution of plutonic rocks in the central Abukuma plateau, northeastern Japan Arc. J Miner Petr Sci 110:145–149
Masui J (1954) Mineralogical studies on the soil genesis (2): the clay minerals in the soil derived from granodiorite at Ogoe, Fukushima Prefecture (I). J Miner Petrol Sci 38:165–176 (In Japanese with English abstract)
Milnes AR, Fitzpatrick RW (1989) Titanium and zirconium minerals. In: Dixon JB, Weed SB (eds) (Co-eds) minerals in soil environments, 2nd edn. Soil Science Society of America, Madison, pp 1131–1205
Mizota C, Aomina S (1975) Clay mineralogy of some volcanic ash soils in which cristobalite predominates. Soil Sci Plant Nutr 21:327–335
Mizuno N, Amano Y, Mizuno T, Nanzyo M (2008) Changes in the heavy minerals content of Tarumae-a tephra with distance from the source volcano and its effect on the element concentration of the tephra. Soil Sci Plant Nutr 54:839–845
Monger HC, Kelly EF (2002) Silica minerals. In: Dixon JB, Schulze DG (eds) (Co-eds) soil mineralogy with environmental applications. Soil Science Society of America, Inc, Madison, pp 611–636
Nanzyo M, Nakamaru Y, Yamasaki S, Samonte HP (1999) Effect of reducing conditions on the weathering of Fe^{3+}-rich biotite in the new lahar depsoit from Mt. Pinatubo, Philippines. Soil Sci 164:206–214
Rhoten FE, Bigham JM, Norton LD, Smeck ME (1981) Contribution of magnetite to oxalate-extractable iron in soils and sediments from the Maumee River basin of Ohio. Soil Sci Soc Am J 45:645–649
Shoji S, Ito T, Saigusa M (1987) Andisol-Entisol transition problem. Pedologist 31:171–175
Skinner BJ, Mruck B (2011) The rock cycle. In: The blue planet an introduction to earth system science, 3rd edn. Wiley, New York, pp 64–71
Soil Survey Staff (1999) Soil taxonomy, a basic system of soil classification of making and interpreting soils surveys, USDA-NRCS, agriculture handbook no. 436, U.S. Government Printing Office, Washington, DC
Thompson M, Ukrainczyk L (2002) Micas. In: Dixon JB, Schulze DG (eds) (Co-eds) soil mineralogy with environmental applications. Soil Science Society of America, Inc, Madison, pp 431–466
Walker (1983) The effect of magnetite on oxalate- and dithionite-extractable iron. Soil Sci Soc Am J 47:1022–1026
Wolfe EW, Hoblitt RP (1996) Overview of the eruption. In: Newhall CG, Punongbayan RS (eds) . Fire and mud, Eruptions and lahars of Mount Pinatubo, Philippines, Plilippine Institute of Volcanology and Seismology/University of Washington Press, Quezon city/Seattle/London, pp 3–20
Wyllie PJ (1971) The structure, petrology, and composition of the earth' crust. In: The dynamic earth: textbook in geoscience. Wiley, New York, pp 139–155